

# ASEAN Journal of Science and Engineering



Journal homepage: <a href="http://ejournal.upi.edu/index.php/AJSE/">http://ejournal.upi.edu/index.php/AJSE/</a>

# Multifaceted Applications of Pyrazole-Based Tetradentate Ligand Coordinated with Transition Metals (Fe, Zn, Co, Cu): Synthesis, Characterization, Catalysis, Antimicrobial Activity, ADMET, and Molecular Docking Insights

Ziloukha Ridal<sup>1</sup>, Zakariae Abbaoui<sup>1</sup>, Hicham Elmsellem<sup>1,2</sup>, Abdelouahed Aouniti<sup>1</sup>, El Bekkaye Yousfi<sup>2</sup>, Mohamed El Kodadi<sup>1,3</sup>, Chahrazad Belkhiri<sup>1</sup>, Faiza Souna<sup>2</sup>, Rachid Touzani<sup>1,\*</sup>, Ahmed A. Elhenawy<sup>4,5</sup>, Belkheir Hammouti<sup>6</sup>

<sup>1</sup>Mohammed First University, Oujda, Morocco
<sup>2</sup>Institute of Nursing and Health Technical Professions, Oujda, Morocco

<sup>3</sup>CRMEF Oriental, Oujda, Morocco

<sup>4</sup>Al-Azhar University, Al-Baha, Egypt

<sup>5</sup>Al-Baha University, Al-Baha, Saudi Arabia

<sup>6</sup>University Euromed of Fez, Fez, Morocco

\*Correspondence: E-mail: r.taozani@ump.ac.ma

# **ABSTRACT**

This study reports the synthesis of a pyrazole-based tetradentate ligand and its coordination with transition metals (iron, zinc, cobalt, and copper) to evaluate catalytic and antimicrobial properties. The ligand was synthesized via condensation reactions and characterized using spectroscopic methods. Coordination with metal salts generated mono- and dinuclear complexes, which were tested for catechol oxidation activity, antimicrobial potential, pharmacokinetic profiles, and molecular docking with Pglycoprotein. Findings revealed that iron complexes, especially the diiron variant, exhibited the highest catalytic efficiency. The free ligand showed strong antifungal activity, while selected metal complexes displayed selective antibacterial effects. These results indicate that metal coordination modulates electronic and structural properties, enhancing redox activity and biological performance. The study provides insights into designing multifunctional compounds for catalytic and therapeutic applications.

#### **ARTICLE INFO**

#### Article History:

Submitted/Received 20 Jun 2025 First Revised 24 Jul 2025 Accepted 04 Sep 2025 First Available online 05 Sep 2025 Publication Date 01 Sep 2026

#### Keyword:

ADMET properties, Antibacterial Antifungal, Catecholase activity, Coordination complexes, Docking, Drug-likness.

© 2026 Universitas Pendidikan Indonesia

#### 1. INTRODUCTION

The World Health Organization has identified microbial infections as one of the greatest global health threats, particularly in developing countries [1]. Addressing this challenge has prompted researchers to explore heterocyclic compounds, which serve as fundamental building blocks in numerous applications across industrial, agricultural, and medical domains [2]. A classic biochemical example involves the oxidation of o-dianisidine (3,3'-dimethoxybenzidine) by hydrogen peroxide in the presence of horseradish peroxidase (HRP), a system once used in glucose detection assays [3]. Inspired by such bio-catalytic mechanisms, recent efforts have focused on organic molecules with versatile functionalities [4].

Among these, pyrazole and its derivatives have emerged as highly promising due to their wide-ranging utility in pharmacology, electronics, coordination chemistry, and corrosion inhibition [5,6]. Pyrazoles exhibit notable cytotoxic, antifungal, and antibacterial properties [7-11], and their function as N-donor ligands enhances their coordination capabilities with transition metals [12,13]. These ligands are valued for their structural flexibility, stability, and strong metal-binding affinity, making them attractive in both catalytic and medicinal chemistry [14].

In particular, Co(II)/pyrazole complexes have shown notable catalytic and pharmacological potential [15]. A key focus in this field involves mimicking metalloenzymes like catechol oxidase, a copper-containing enzyme found in plants, fungi, and bacteria. This enzyme catalyzes the oxidation of o-diphenols to o-quinones, which subsequently polymerize into dark pigments involved in plant browning [16]. From a biomedical standpoint, such enzymatic mimicry holds relevance for addressing infections caused by pathogenic microbes. For instance, Listeria monocytogenes, a Gram-positive bacterium, causes invasive listeriosis in vulnerable populations, including the elderly, pregnant women, and immunocompromised individuals. Similarly, Staphylococcus aureus—asymptomatically carried by about 30% of humans—can cause bacteraemia, endocarditis, osteoarticular infections, and device-related complications [17].

Considering these health concerns, the development of heterocyclic-based antimicrobial agents becomes increasingly vital. Pyrazole derivatives, due to their multifunctionality, stand out as central candidates in the rational design of such agents. Their ability to form stable complexes with transition metals enables the fine-tuning of redox and biological behavior, bridging synthetic chemistry with therapeutic innovation. Transition metal complexes of pyrazole ligands are especially promising for emulating enzymatic activities like catecholase catalysis, contributing to both biomedical and green chemistry pursuits.

Therefore, the synthesis of pyrazole-based tetradentate ligands and their coordination with metals such as Fe(II), Zn(II), Co(II), and Cu(II) offers a strategic platform to study structure—activity relationships, catalytic dynamics, and pharmacokinetic behavior. Coordination with these metals has been shown to enhance biological interactions and redox potential, opening new avenues for developing effective antimicrobial agents against drugresistant pathogens. In light of these considerations, this study aims to bridge molecular design with functional application by synthesizing and characterizing novel pyrazole-based metal complexes. Through kinetic, structural, and biological evaluation, we seek to generate insights that support the rational optimization of these systems for catalytic and therapeutic deployment.

#### 2. METHODS

# 2.1. Synthesis of Tetradentate Ligand (Ligand 3)

**Figure 1** shows the synthesis method. The synthesis of  $N^4$ ,  $N^4$ ,  $N^4$ ,  $N^4$ ',  $N^4$ '-tetrakis((3,5-dimethyl-1H-pyrazol-1-yl) methyl)-3,3'-dimethoxy-[1,1'-biphenyl]-4,4'-diamine (Ligand 3) was performed in a 250 mL round-bottom flask equipped with a magnetic stirrer. A solution containing four equivalents of 1-hydroxymethyl-3,5-dimethylpyrazole in 40 mL of acetonitrile was combined with one equivalent of o-dianisidine in 20 mL of the same solvent. The reaction mixture was stirred at room temperature for four days, leading to the precipitation of the crude product. This solid was filtered, dried over MgSO<sub>4</sub>, and purified through recrystallization or liquid–liquid extraction to yield the final ligand as a white solid [18]. The compound was obtained with a yield of 13.07% and a melting point of 125 °C.

For detailed information regarding Ligand 3, this compound was obtained yield 13.07 %, MP: 125 °C, FT-IR: (KBr, v(cm<sup>-1</sup>): exhibited characteristic absorption bands corresponding to CH stretching vibrations in the range of 2820–3000 cm<sup>-1</sup>, C=C stretching vibrations in the range of 1400–1630 cm<sup>-1</sup>, and C-O stretching vibrations in the range of 1130–1286 cm<sup>-1</sup>. The UV-Visible spectrum displayed absorption maxima ( $\lambda_{max}$ ) at 310 nm ( $\epsilon$  = 1181.5 L.mol<sup>-1</sup>.cm<sup>-1</sup>) and 335 nm ( $\epsilon$  = 1340.L.mol<sup>-1</sup>.cm<sup>-1</sup>). The <sup>1</sup>H NMR spectrum (DMSO-d<sub>6</sub>, 300 MHz) revealed distinct signals:  $\delta$  2.30 ppm (s, 3H, N=C-CH<sub>3</sub>),  $\delta$  2.52 ppm (s, 3H, N-C-CH<sub>3</sub>),  $\delta$  3.85 ppm (s, 3H, O-CH<sub>3</sub>),  $\delta$  5.55 ppm (s, 2H, N-CH<sub>2</sub>-N),  $\delta$  6.10 ppm (s, 1H, c=CH-C),  $\delta$  6.70 ppm (d, 1H, aromatic),  $\delta$  6.95 ppm (d, 1H, aromatic), and  $\delta$  7.00 ppm (s, 1H, aromatic). The <sup>13</sup>C NMR spectrum (DMSO-d<sub>6</sub>, 400 MHz) further confirmed the structure with signals at  $\delta$  13.5 ppm (N=C-CH<sub>3</sub>),  $\delta$  11 ppm (N-C-CH<sub>3</sub>),  $\delta$  55.8 ppm (O-CH<sub>3</sub>),  $\delta$  58 ppm (N-CH<sub>2</sub>-N),  $\delta$  148 ppm (N=C-CH<sub>3</sub>),  $\delta$  105 ppm (N=C-CH=C),  $\delta$  140 ppm (N-C-CH<sub>3</sub>), and aromatic carbons in the range of 112.5–146 ppm.

**Figure 1.** Synthesis of the tetradentate pyrazole-based ligand 3.

Characterization was carried out using FT-IR, UV-Vis,  $^1H$  NMR, and  $^{13}C$  NMR spectroscopy. FT-IR spectra showed CH stretching (2820–3000 cm $^{-1}$ ), C=C stretching (1400–1630 cm $^{-1}$ ), and C=O stretching (1130–1286 cm $^{-1}$ ). UV-Vis absorption maxima appeared at 310 nm and 335 nm.  $^1H$  NMR (DMSO-d<sub>6</sub>, 300 MHz) revealed peaks typical of methyl, methoxy, methylene, and aromatic protons.  $^{13}C$  NMR further confirmed the structure with signals corresponding to methyl, methoxy, methylene, and aromatic carbons.

# 2.2. Synthesis of Metal Complexes (4-8)

**Figure 2** shows the synthesis of metal complexes. Ligand 3 was reacted with metal salts  $(FeCl_2, ZnCl_2, Co(NO_3)_2 \cdot 6H_2O)$ , and  $CuCl_2 \cdot 2H_2O)$  in methanol under constant stirring at room

temperature for four days. The resulting precipitates were filtered and dried over MgSO<sub>4</sub> to obtain the corresponding complexes.

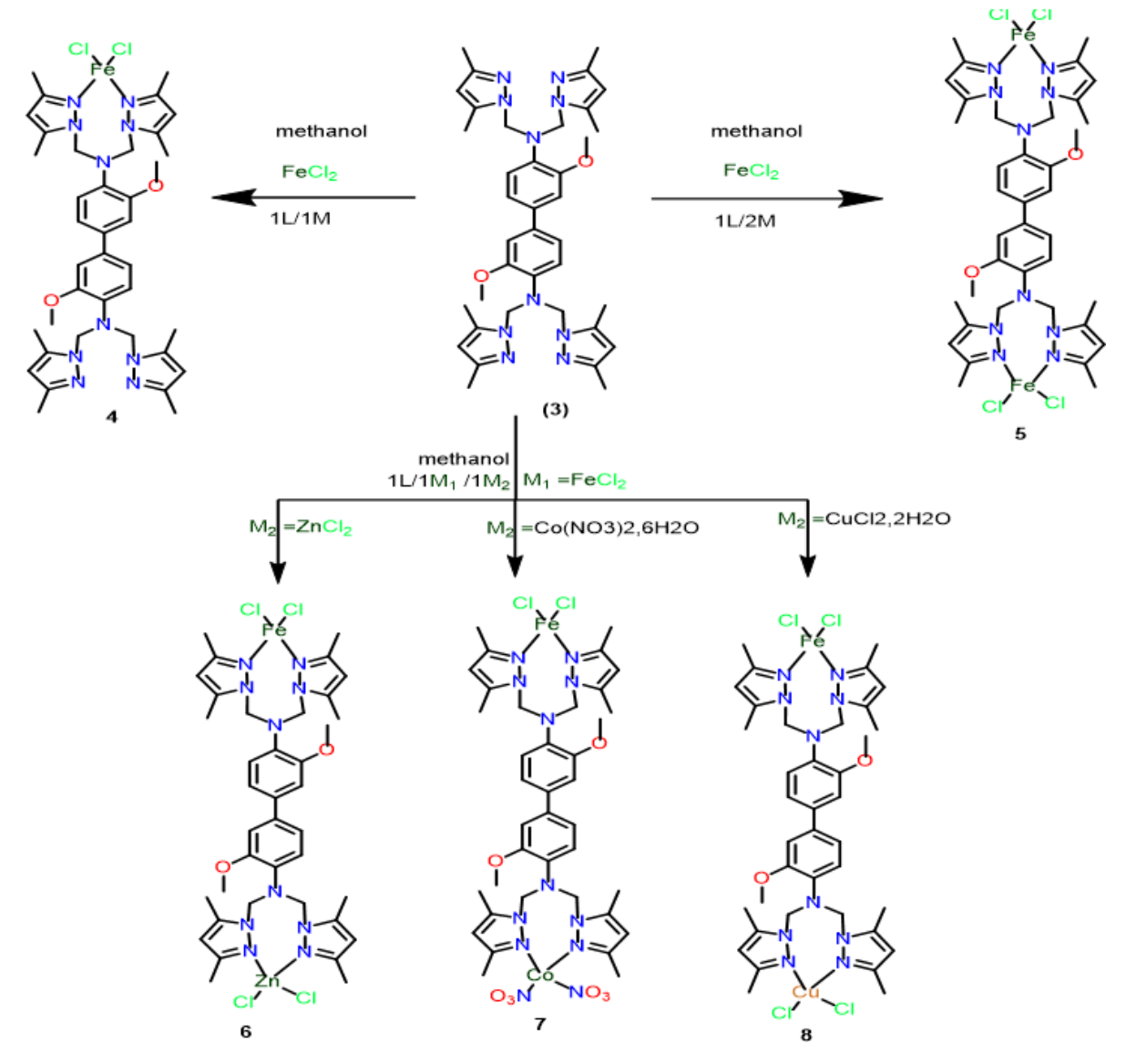


Figure 2. Synthesis of ligand 3 and its complexes with Fe<sup>2+</sup>, Zn<sup>2+</sup>, Co<sup>2+</sup>, and Cu<sup>2+</sup> salts.

Each complex was characterized using FT-IR and UV-Vis spectroscopy (see Figure 3):

- (i) Mono Fe-Complex (4): IR bands observed at 3156–3360 cm<sup>-1</sup> and 2516–2845 cm<sup>-1</sup>; UV-Vis absorptions ranged from 320 to 485 nm.
- (ii) Di Fe-Complex (5): IR bands between 3189–3440 cm<sup>-1</sup>; UV-Vis absorptions from 340 to 420 nm.
- (iii) Zn-Complex (6): IR bands from 3182–3433 cm<sup>-1</sup>; UV-Vis absorptions from 210 to 435 nm.
- (iv) Co-Complex (7): IR bands at 3064–3552 cm<sup>-1</sup>; UV-Vis absorptions at 300–435 nm.
- (v) Cu-Complex (8): IR bands from 2958–3492 cm<sup>-1</sup>; UV-Vis absorption observed at 295 nm. New absorption peaks between 2900 and 3100 cm<sup>-1</sup> confirmed alkane-related vibrations, indicating successful complexation.

Detailed information regarding several chemicals obtained is in the following:

(i) Mono Fe-Complex (4): was characterized by FT-IR spectroscopy, which revealed absorption bands in the ranges of 3156–3360 cm<sup>-1</sup>, 2516–2845 cm<sup>-1</sup>, and specific peaks at 1586, 1493, 1460, 1401, 1269, 1169, 1031, and 800 cm<sup>-1</sup>. The UV-Visible spectrum

- exhibited multiple absorption maxima at 320 nm ( $\epsilon$  = 1940 L.mol<sup>-1</sup>.cm<sup>-1</sup>), 340 nm ( $\epsilon$  = 2041 L.mol<sup>-1</sup>.cm<sup>-1</sup>), 360 nm ( $\epsilon$  = 2073.5 L.mol<sup>-1</sup>.cm<sup>-1</sup>), 380 nm ( $\epsilon$  = 2060 L.mol<sup>-1</sup>.cm<sup>-1</sup>), 390 nm ( $\epsilon$  = 2087 L.mol<sup>-1</sup>.cm<sup>-1</sup>), 410 nm ( $\epsilon$  = 2169.5 L.mol<sup>-1</sup>.cm<sup>-1</sup>), 420 nm ( $\epsilon$  = 2304.5 L.mol<sup>-1</sup>.cm<sup>-1</sup>), 445 nm ( $\epsilon$  = 2304 L.mol<sup>-1</sup>.cm<sup>-1</sup>), and 485 nm ( $\epsilon$  = 2128 L.mol<sup>-1</sup>.cm<sup>-1</sup>).
- (ii) Di Fe-Complex (5): was characterized by FT-IR spectroscopy, which revealed absorption bands in the ranges of 3189-3440 cm<sup>-1</sup>, 2813-2958 cm<sup>-1</sup>, and specific peaks at 1566-1592 cm<sup>-1</sup>, 1447-1532 cm<sup>-1</sup>, 1401 cm<sup>-1</sup>, 1117-1308 cm<sup>-1</sup>, 1031, 767-846 cm<sup>-1</sup>, 583 cm<sup>-1</sup>. The UV-Visible spectrum exhibited multiple absorption maxima at 340 nm ( $\epsilon$  = 1854 L.mol<sup>-1</sup>.cm<sup>-1</sup>), 345 nm ( $\epsilon$  = 1897 L.mol<sup>-1</sup>.cm<sup>-1</sup>); 360 nm ( $\epsilon$  = 1950 L.mol<sup>-1</sup>.cm<sup>-1</sup>); 390 nm ( $\epsilon$  = 1933.5 L.mol<sup>-1</sup>.cm<sup>-1</sup>); 410 nm ( $\epsilon$  = 1950.5 L.mol<sup>-1</sup>.cm<sup>-1</sup>); 420 nm ( $\epsilon$  = 1957.5 L.mol<sup>-1</sup>.cm<sup>-1</sup>); 415 nm ( $\epsilon$  = L.mol<sup>-1</sup>.cm<sup>-1</sup>).
- (iii) Zn-Complex (6): was characterized by FT-IR spectroscopy, which revealed absorption bands in the ranges of 3182-3433 cm<sup>-1</sup>, 2813-2971 cm<sup>-1</sup>, and specific peaks at 1374-1486 cm<sup>-1</sup>, 1018 cm<sup>-1</sup>, 615 cm<sup>-1</sup>. The UV-Visible spectrum exhibited multiple absorption maxima at 210 nm ( $\epsilon$  = 46 L.mol<sup>-1</sup>.cm<sup>-1</sup>), 225 nm ( $\epsilon$  = 41 L.mol<sup>-1</sup>.cm<sup>-1</sup>), 235 nm ( $\epsilon$  = 44.5 L.mol<sup>-1</sup>.cm<sup>-1</sup>), 250 nm ( $\epsilon$  = 51 L.mol<sup>-1</sup>.cm<sup>-1</sup>), 260 nm ( $\epsilon$  = L.mol<sup>-1</sup>.cm<sup>-1</sup>), 275 nm ( $\epsilon$  = 47 L.mol<sup>-1</sup>.cm<sup>-1</sup>), 430 nm ( $\epsilon$  = 96 L.mol<sup>-1</sup>.cm<sup>-1</sup>).
- (iv) *Co-Complex (7)*: was characterized by FT-IR spectroscopy, which revealed absorption bands in the ranges of 3064-3552 cm<sup>-1</sup>, and specific peaks at 1605-1671 cm<sup>-1</sup>, 1249-1519 cm<sup>-1</sup>, 1024 cm<sup>-1</sup>, 576 cm<sup>-1</sup>. The UV-Visible spectrum exhibited multiple absorption maxima at 300 nm ( $\epsilon$  = 223 L.mol<sup>-1</sup>.cm<sup>-1</sup>), 315 nm ( $\epsilon$  = 219.5 L.mol<sup>-1</sup>.cm<sup>-1</sup>), 320 nm ( $\epsilon$  = 219. L.mol<sup>-1</sup>.cm<sup>-1</sup>), 435 nm ( $\epsilon$  = 388.5 L.mol<sup>-1</sup>.cm<sup>-1</sup>).
- (v) *Cu-Complex (8)*: was characterized by FT-IR spectroscopy, which revealed absorption bands in the ranges of 2958-3492 cm<sup>-1</sup>, and specific peaks at 1586 cm<sup>-1</sup>, 1236 cm<sup>-1</sup>, 820 cm<sup>-1</sup>, 661 cm<sup>-1</sup>. The UV-Visible spectrum exhibited multiple absorption maxima at 295 nm ( $\epsilon$  = 303.5 L.mol<sup>-1</sup>.cm<sup>-1</sup>).

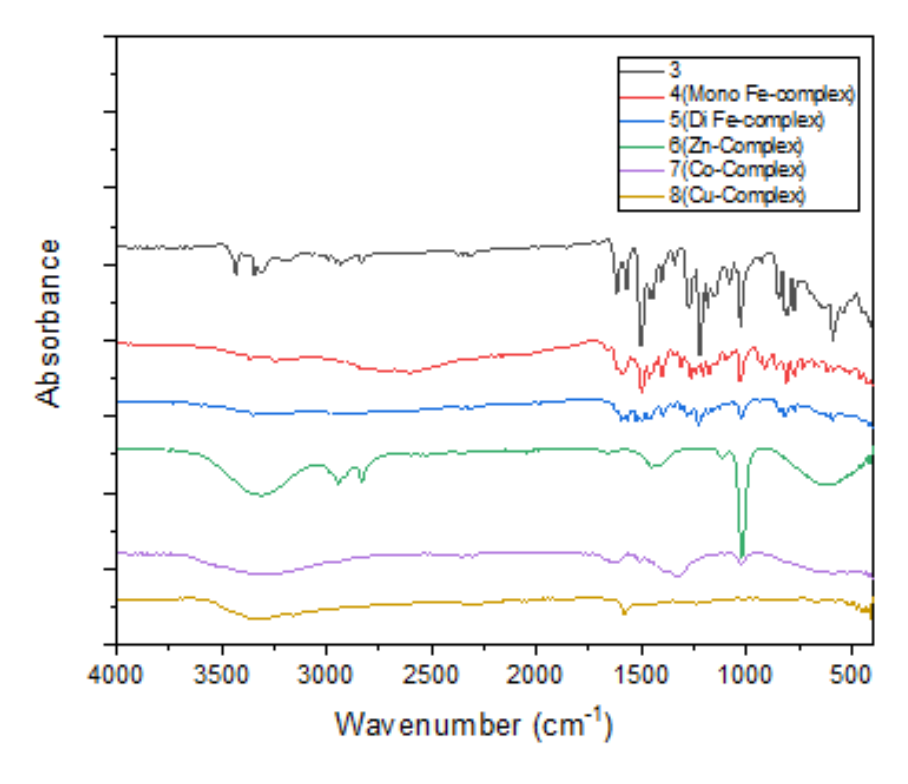


Figure 3. FT-IR spectrum of ligand 3 and its metal complexes (4-8).

#### 2.3. Catalytic Oxidation of Catechol

The catalytic activity was assessed based on catechol oxidation, monitored by UV-Vis spectrophotometry through the increase in quinone absorbance [19-22]. The oxidation mimics catechol oxidase activity, which is of biological significance due to the presence of copper enzymes in natural systems [23,24] (Moiseeva and Butin 2005; Groysman and Holm 2009; Holland, Tolman, and Se 2000). Copper enzymes are classified into three major types (I, II, and III), each with distinct biological roles such as electron transfer and oxygen transport [25]. These insights inform the understanding of metal-ligand interactions relevant to redox catalysis and metabolic regulation [26,27].

#### 2.4. Prepation of Test Solutions

Stock solutions were prepared by dissolving 1 mg of each compound in 1 mL of DMSO to obtain 1 mg/mL solutions [28,29].

# 2.5. Antimicrobial Assay and MIC Determination

Microbial inocula were prepared by suspending 2–3 colonies from fresh cultures in sterile physiological saline. After vortexing, turbidity was adjusted to 0.5 McFarland standard [30,31]. Antimicrobial tests were performed using serial dilutions of each compound inoculated with standardized microbial suspensions. After incubation, the minimum inhibitory concentration (MIC) was determined as the lowest concentration that inhibited 90% of microbial growth [32-34].

# 2.6. Molecular Docking Protocol

Docking studies were conducted using the Glide module to evaluate the binding interactions of the ligand and metal complexes with the P-glycoprotein target (PDB ID: 4Z2D). Binding affinities and interaction modes were compared against a standard inhibitor as reference [35]. These analyses aimed to correlate structural features with biological potential.

#### 3. RESULTS AND DISCUSSION

The design of the ligand takes advantage of electron-donating methoxy groups and a rigid biphenyl backbone to stabilize transition metal centers, a strategy comparable to phenanthroline-based frameworks [36]. The formation of mono- versus dinuclear complexes appears to be influenced by steric hindrance and the ionic radius of the metal, as evidenced by the distinct coordination behaviors observed for Fe and Zn systems. Ligand 3 was synthesized through a nucleophilic substitution reaction between a 3,5-dimethylpyrazole derivative (1) and o-dianisidine (2) in acetonitrile. The moderate yield (13.07%) may be attributed to steric congestion from the bulky pyrazole moieties or competing side reactions—challenges often encountered in the synthesis of multidentate ligands [37].

FT-IR analysis revealed C–H stretching (2820–3000 cm<sup>-1</sup>) and C–O stretching (1130–1286 cm<sup>-1</sup>) bands, confirming the presence of methoxy and pyrazole groups. The absence of O–H vibrations indicated full substitution at the amine positions. The <sup>1</sup>H NMR spectrum displayed a singlet at  $\delta$  5.55 ppm (N–CH<sub>2</sub>–N) and aromatic signals between  $\delta$  6.70–7.00 ppm, validating the symmetric biphenyl framework. Methyl ( $\delta$  2.30 and 2.52 ppm) and methoxy ( $\delta$  3.85 ppm) groups aligned with the proposed structure. UV-Visible absorptions at 310 and 335 nm ( $\epsilon$  ≈ 1181–1340 L·mol<sup>-1</sup>·cm<sup>-1</sup>) were attributed to  $\pi$ – $\pi$ \* transitions within the aromatic and pyrazole domains, consistent with extended conjugation [31].

The ligand was subsequently coordinated with FeCl<sub>2</sub>, ZnCl<sub>2</sub>, Co(NO<sub>3</sub>)<sub>2</sub>·6H<sub>2</sub>O, and CuCl<sub>2</sub>·2H<sub>2</sub>O at ambient temperature. Its tetradentate nature facilitated binding via pyrazole nitrogen atoms and possibly methoxy oxygen atoms, yielding mono- and dinuclear complexes (Schemes 1–2). In the mono Fe-complex (4), FT-IR showed shifts in C–H (3156–3360 cm<sup>-1</sup>) and C–O (1269 cm<sup>-1</sup>) regions, indicating coordination. UV-Vis spectroscopy revealed multiple absorption bands (320–485 nm), indicative of d–d transitions and ligand-to-metal charge transfer (LMCT) typical of high-spin Fe(II) octahedral complexes [36].

The di-Fe complex (5) exhibited broader IR bands (3189–3440 cm<sup>-1</sup>) and a split UV-Vis profile (340–420 nm), suggesting a binuclear configuration with bridging ligands, a feature consistent with related Fe(II) systems. The Zn complex (6) presented simplified UV absorptions (210–435 nm) and IR signals between 1374–1486 cm<sup>-1</sup>, indicative of a tetrahedral geometry, where ligand field effects are comparatively subdued (Masoud et al. 2023). For the Co complex (7), an intense UV-Vis band at 435 nm ( $\varepsilon$  = 388.5 L·mol<sup>-1</sup>·cm<sup>-1</sup>) reflected d–d transitions in an octahedral Co(II) environment, while IR shifts (1605–1671 cm<sup>-1</sup>) suggested coordination via pyrazole nitrogen atoms [36]. The Cu complex (8) showed a broad UV-Vis band centered at 295 nm ( $\varepsilon$  = 303.5 L·mol<sup>-1</sup>·cm<sup>-1</sup>), likely due to LMCT or a distorted square-planar geometry, as observed in other Cu(II)-pyrazole systems [37].

Comparative analysis with Schiff base analogs revealed that pyrazole ligands exhibit stronger  $\sigma$ -donor properties, improving metal–ligand bond stability. Furthermore, the absence of imine linkages in ligand 3 eliminates hydrolytic vulnerability, a known limitation of Schiff base structures.

The catalytic oxidation of catechol was monitored by observing the progressive increase in absorbance corresponding to quinone formation using UV-Vis spectrophotometry. As shown in **Figure 4**, the catechol substrate and metal complex solution were introduced into the spectrophotometric cell at 25 °C. The characteristic rise in absorbance at 390 nm over time confirmed the generation of o-quinone and enabled kinetic analysis of the catecholase-like activity.

Figure 4. Model catecholase reaction with the ligands and metals used.

Kinetic measurements of catechol oxidation were performed in methanol using metal complexes derived from ligand 3 with FeCl<sub>2</sub>, ZnCl<sub>2</sub>, Co(NO<sub>3</sub>)<sub>2</sub>·6H<sub>2</sub>O, and CuCl<sub>2</sub>·2H<sub>2</sub>O. The evolution of absorbance over time was recorded spectrophotometrically, allowing for a comparative assessment between in situ-generated complexes and their pre-synthesized counterparts (**Table 1**). The corresponding reaction profiles are presented in **Figure 5**.

The analysis focused on comparing complexes 4 through 8 in terms of catalytic behavior, highlighting three critical factors: reaction kinetics, metal identity, and preparation method. Notably, in situ complexes exhibited markedly superior catalytic efficiency relative to their

isolated analogues. This was demonstrated by higher absorbance values over the reaction duration, indicating more effective catechol oxidation.

Among all tested systems, the in situ di-Fe complex (5) displayed the highest catalytic activity, reaching a maximum absorbance of 4.12 at 3600 seconds, closely followed by mono-Fe complex (4) with 4.10. In contrast, complexes 8 (Cu), 6 (Zn), and 7 (Co) showed moderate activity, with absorbance maxima of 3.67, 2.41, and 2.01, respectively.

Pre-synthesized complexes exhibited substantially reduced performance. Although complex 5 (di-Fe) remained the most active among this group, its maximum absorbance dropped to 3.02. The mono-Fe complex (4) followed with 2.78. Other complexes (8 (Cu), 6 (Zn), and 7 (Co)) demonstrated significantly diminished catalytic activity, achieving absorbance values of only 1.27, 0.83, and 0.63, respectively.

These findings suggest that the in-situ generation of metal complexes enhances substrate accessibility and electron transfer efficiency, likely due to the absence of crystal packing constraints and increased structural flexibility. This enhancement supports previous observations on the influence of coordination environment on metalloenzyme mimics [24,25].

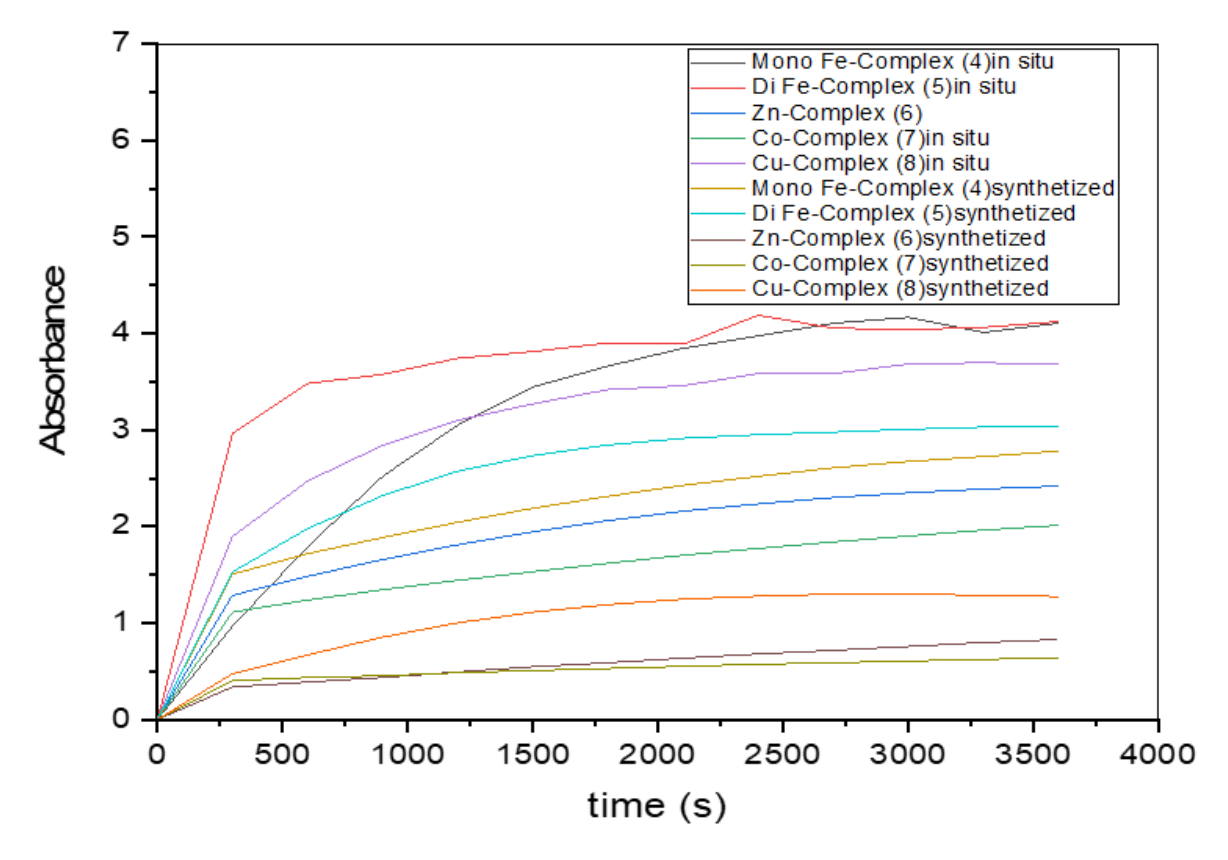


Figure 5. Oxidation of catechol in the presence of ligand 3 with the metal salt FeCl<sub>2</sub>, ZnCl<sub>2</sub>, Co(NO<sub>3</sub>)<sub>2</sub>: 6H<sub>2</sub>O, CuCl<sub>2</sub>,: 2H<sub>2</sub>O complex in situ and complex synthesized.

**Table 1.** Catechol oxidation rates for 5 complexes synthesized and 5 complexes in situ in methanol.

Complex	V <sub>max</sub>	b	а	Т
	(μmol/L min)	(µmol/mL.min)	(µmol/mg.min)	(min <sup>-1</sup> )
4 (mono Fe-Complex)	28.96	222.00	138.12	110995.99
5 (di Fe-Complex)	31.55	241.89	129.99	120937.49
6 (Zn-Complex)	8.64	66.28	35.25	33131.47
7 (Co-Complex)	6.64	50.95	25.82	25472.97
8 (Cu-Complex)	13.27	101.74	54.22	50861.61
4 (mono Fe-Complex)	42.77	327.90	204.01	163942.43
5 (di Fe-Complex)	42.92	329.10	176.86	164541.70
6 (Zn-Complex)	25.19	193.18	102.76	96586.17
7 (Co-Complex)	20.96	160.76	73.42	80369.20
8 (Cu-Complex)	38.31	293.72	150.76	146855.31

Several points regarding comparative analysis of catalytic parameters and metal types are in the following:

- (i) Catalytic Parameters. The kinetic parameters (maximum reaction velocity (Vmax) and Michaelis-Menten constant (Km)) further illustrate the contrasting performance between in situ and pre-synthesized metal complexes in catalyzing catechol oxidation. Among the in situ systems, the di-Fe complex (5) exhibited the highest catalytic efficiency, reaching a Vmax of 42.92 μmol/L·min, followed closely by the mono-Fe complex (4) with 42.77 μmol/L·min. Other in situ complexes displayed lower efficiency: Cu (8) at 38.31, Zn (6) at 25.19, and Co (7) at 20.96 μmol/L·min. In contrast, the pre-synthesized complexes revealed significantly reduced catalytic activities. Di-Fe (5) and mono-Fe (4) complexes retained relatively high Vmax values of 31.55 and 28.96 μmol/L·min, respectively, although these values were notably lower than those of their in situ counterparts. The Zn (6), Co (7), and Cu (8) complexes demonstrated markedly diminished catalytic activity, with Vmax values of only 8.64, 6.64, and 13.27 μmol/L·min, respectively. These findings emphasize the significant role of preparation method and complex structure in enhancing catalytic turnover [38,39].
- (ii) Comparison of Metal Types. The catalytic efficiency is also profoundly influenced by the identity of the coordinated metal center. Among all tested systems, iron-based complexes, particularly the di-Fe complex (5), consistently outperformed other metals in catalysis. This enhanced performance is likely due to iron's ability to form dual active sites, which facilitate electron transfer and substrate activation during the oxidation process. Copper (Cu), represented by complex 8, exhibited moderate catalytic performance, balancing electron transfer capabilities and coordination behavior, but falling short of the catalytic levels achieved by iron. In contrast, zinc (Zn) and cobalt (Co) complexes demonstrated the lowest catalytic efficiencies. This may be attributed to less favorable coordination geometries or insufficient redox potential, which can hinder effective substrate activation and product release [31].

Taken together, the data suggest that both metal identity and synthesis route play pivotal roles in modulating catalytic behavior. In situ preparation enhances structural flexibility and substrate accessibility, making it the preferred method for generating high-activity catalysts. Among all systems studied, in situ di-Fe (5) and mono-Fe (4) complexes emerge as the most promising candidates for catechol oxidation.

The progressive increase in absorbance at 390 nm—corresponding to o-quinone formation—confirms the oxidative transformation of catechol. This gradual spectral shift, more pronounced in in situ complexes, further underscores their superior catalytic efficiency.

**Figure 6** depicts the absorption spectra of both the in-situ complex and the synthesized complex across varying wavelengths, recorded through UV-Visible scans taken every 10 minutes over one hour. The absorption band associated with o-quinone shows a gradual increase over time, peaking at 390 nm. This progressive change in absorption highlights the enhanced efficiency of the oxidation reaction.

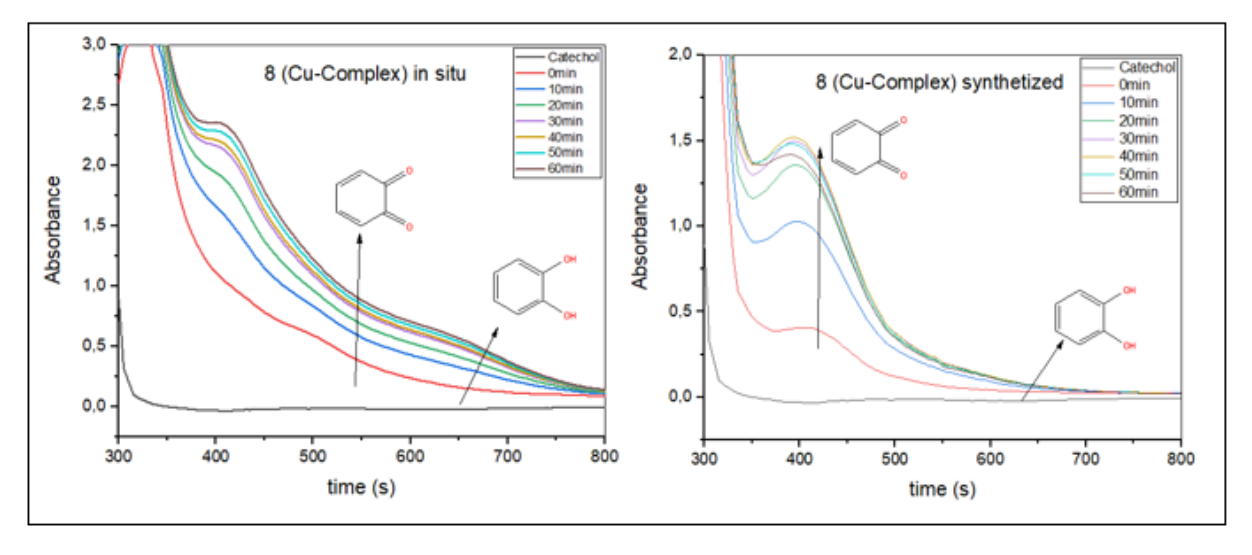


**Figure 6.** O-quinone time-dependent absorption spectrum in the presence of complex 8 (Cucomplex) in situ and synthesized.

UV-Vis spectrophotometric analysis revealed distinct differences in catalytic behavior between synthesized and in situ complexes. As shown in **Figure 6**, the mono-Fe complex (whether prepared in situ or pre-synthesized) exhibited a notable increase in absorbance at 390 nm, indicating effective conversion of catechol to o-quinone. However, the in-situ complex demonstrated a more rapid and sustained absorbance increase, suggesting enhanced catalytic efficiency.

This improved performance is attributed to better molecular interactions during in situ complexation, which likely facilitate optimal alignment of the metal center and substrate, thereby accelerating the oxidation process. In contrast, the synthesized complexes showed comparatively lower catalytic activity, possibly due to conformational rigidity or suboptimal coordination geometries under reaction conditions. These findings underscore the advantages of in situ preparation for catalytic systems, as also supported by recent literature.

The catalytic reactions conformed to Michaelis-Menten kinetics, and this behavior was further validated through Lineweaver-Burk plots, which established the linear relationship between reciprocal substrate concentration and reaction rate (see **Figure 7**).

Several results regarding kinetic and catalytic performance of selected complexes are in the following:

(i) Initial Reaction Rates ( $V_0$ ). The initial reaction rates ( $V_0$ ) for complexes 4 (mono-Fe), 6 (Zn), and 7 (Co) were analyzed as a function of substrate concentration to evaluate their catalytic efficiency in catechol oxidation. Complex 4 (mono-Fe) demonstrated the highest catalytic activity among the three, with a linear increase in  $V_0$  as substrate concentration rose. Its maximum initial rate reached  $8.63 \times 10^{-4}$  mol/L·min at a substrate concentration of 0.2 mol/L, reflecting its effective catalytic behavior. In contrast, complex 6 (Zn) showed

- a considerably lower maximum  $V_0$  of  $3.56 \times 10^{-5}$  mol/L·min, observed at a higher substrate concentration of 0.6 mol/L, indicating reduced catalytic performance. Complex 7 (Co) exhibited intermediate activity with a  $V_0$  of  $7.00 \times 10^{-5}$  mol/L·min at 0.8 mol/L, surpassing Zn but still well below Fe-based performance [16].
- (ii) Michaelis–Menten Kinetics. Kinetic analysis was further carried out using Lineweaver–Burk plots to determine the Vmax and Km values of the complexes. For complex 4 (mono-Fe), a Vmax of  $7.80 \times 10^{-4}$  mol/L·min and a low Km of  $2.11 \times 10^{-4}$  mol/L were recorded, indicating both high catalytic efficiency and strong substrate affinity. Complex 6 (Zn) showed a significantly reduced Vmax of  $3.73 \times 10^{-5}$  mol/L·min and a relatively high Km of  $5.11 \times 10^{-3}$  mol/L, suggesting a weaker interaction with the catechol substrate and diminished catalytic power. Meanwhile, complex 7 (Co) demonstrated moderate kinetics with Vmax =  $6.43 \times 10^{-5}$  mol/L·min and Km =  $5.79 \times 10^{-4}$  mol/L, reflecting intermediate efficiency and binding affinity. All kinetic models exhibited R² values greater than 0.90, confirming strong data conformity to the Michaelis–Menten model.
- (iii) Comparative Kinetic Analysis. A comparative summary of catalytic parameters revealed significant differences among the three complexes. Complex 4 (mono-Fe) clearly outperformed the others with the highest Vmax and the lowest Km, denoting superior catalytic efficiency and strong substrate binding. Conversely, complex 6 (Zn) was the least active, showing both the lowest Vmax and highest Km, indicative of poor catalytic behavior. Complex 7 (Co) positioned itself between the two, with intermediate values of both kinetic parameters. The correlation between Vmax and Km across these complexes also proved consistent, with values ranging from 0.43 to 0.48, validating the observed trends and supporting the reliability of the catalytic efficiency profile for each system.

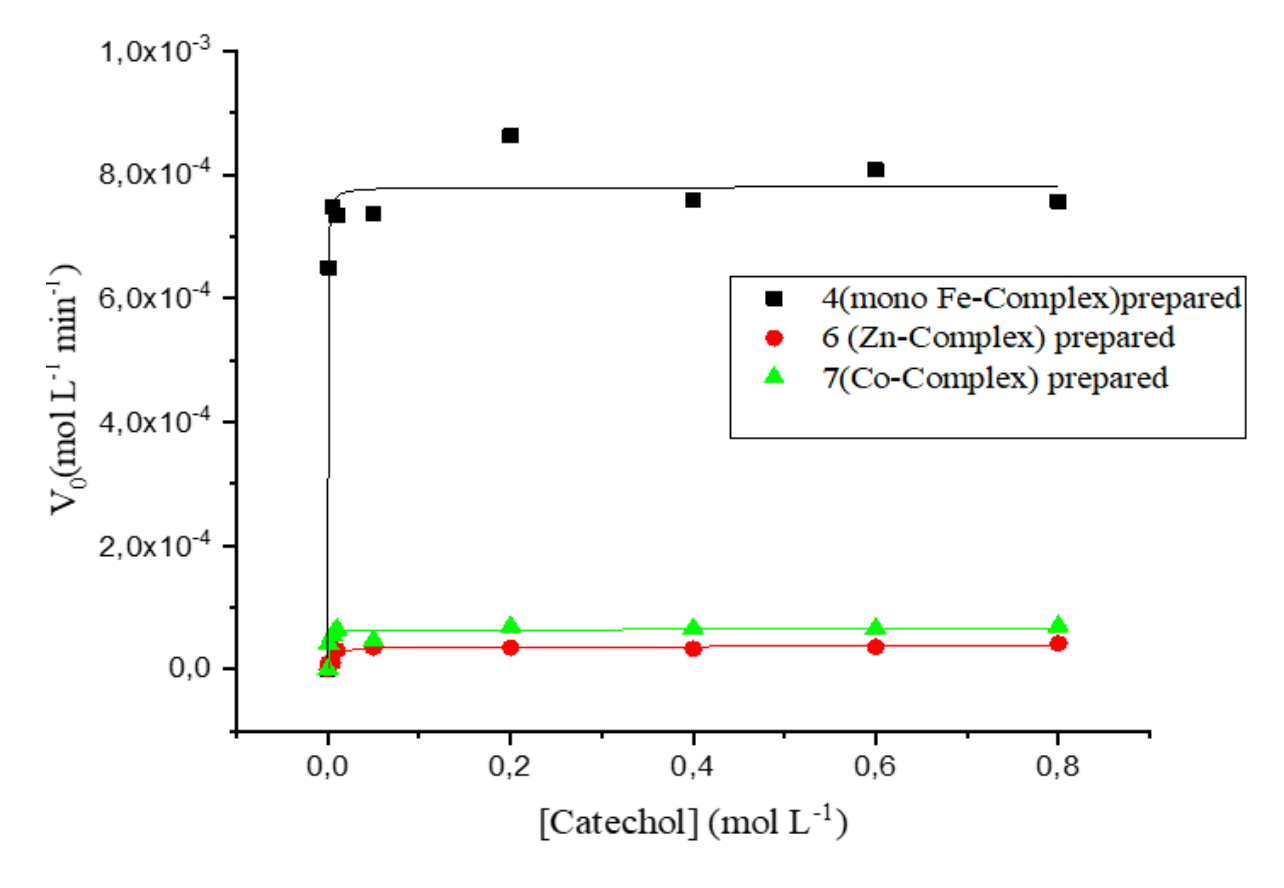


**Figure 7.** Dependence of the reaction rates on the catechol concentrations varying by the complexes prepared (4, 6, and 7).

The antifungal properties of the synthesized ligand and its metal complexes were evaluated against Fusarium oxysporum f.sp. albedinis, a pathogenic fungus that causes significant agricultural damage, particularly in palm groves. Inhibition rates were assessed at three concentrations—50  $\mu$ L, 100  $\mu$ L, and 150  $\mu$ L—using standard in vitro methods. The results, summarized in **Table 2**, reveal a concentration-dependent inhibitory effect, with the free ligand displaying notable antifungal activity. Among the complexes, the Fe-based compounds showed moderate inhibition, whereas the Zn, Co, and Cu complexes exhibited lower effectiveness.

**Table 2.** Rate of inhibition of the growth of Fusarium Oxysporum Fsp. Albedinis according to the concentration of the compounds tested.

	50μL	100μL	150 μL	% inhibition= 100x(D°-Dx) /D°				
Compounds tested	Diameter (cm)	Diameter (cm)	Diameter (cm)	50μL	100μL	150 μL		
3 (Ligand)	6.20	5.00	3.80	17.30	33.30	49.30		
4 (mono Fe-Complex)	7.50	6.00	5.50	0.00	20.00	26.60		
5 (di Fe-Complex)	7.50	7.20	7.20	0.00	4.00	4.00		
6 (Zn-Complex)	7.50	7.00	7.00	0.00	6.66	6.66		
7 (Co-Complex)	7.30	7.00	6.50	2.66	6.66	13.33		
8 (Cu-Complex)	7.20	7.00	7.00	4.00	6.66	6.66		

The antifungal activities of ligand 3 and its metal complexes were assessed by measuring the fungal growth diameters and calculating percentage inhibition, as presented in **Table 2**. The results indicated varying levels of antifungal potency across the tested compounds.

Ligand 3 demonstrated the strongest antifungal activity, with inhibition rates increasing proportionally with concentration: from 17.3% at 50  $\mu$ L to 49.3% at 150  $\mu$ L. This suggests that the free ligand retains essential functional groups necessary for antifungal action, likely through enhanced interaction with fungal cell walls or membranes.

Complex 4 (mono-Fe) exhibited moderate antifungal efficacy, reaching 20.0% inhibition at 100  $\mu$ L and 26.6% at 150  $\mu$ L. These findings imply that coordination with Fe(II) partially enhances the antifungal potential, although not to the extent observed with the free ligand. In contrast, complex 5 (di-Fe) showed significantly lower activity, with only 4.0% inhibition at both 100  $\mu$ L and 150  $\mu$ L. The diminished activity may be due to steric hindrance or reduced accessibility of active sites caused by dinuclear coordination.

Complexes 6 (Zn) and 8 (Cu) both yielded weak antifungal effects, maintaining consistent inhibition of 6.66% at higher concentrations. This suggests limited interaction between the complexes and fungal targets, potentially due to unfavorable binding geometries or low membrane permeability. Complex 7 (Co) showed a slight improvement with increasing dose, rising from 2.66% at 50  $\mu$ L to 13.33% at 150  $\mu$ L. However, overall antifungal efficacy remained low.

These results reinforce previous findings that coordination can modulate biological activity: while mono-Fe coordination (complex 4) enhances antifungal performance, excessive coordination (complex 5) or coordination with less reactive metals (Zn, Co, Cu) tends to diminish it [11,28]. The data suggest that the free ligand outperforms all metal complexes, and that mononuclear iron complexes strike the optimal balance between structural integrity and biological activity.

The antibacterial properties of ligand 3 and its corresponding metal complexes (4 to 8) were tested against a panel of both Gram-positive and Gram-negative bacterial strains, specifically Staphylococcus aureus, Salmonella, Listeria monocytogenes, and Escherichia coli. Evaluation was carried out by measuring zones of inhibition on agar plates and determining the minimum inhibitory concentration (MIC) for each compound.

**Table 3** presents the measured inhibition zone diameters for ligand 3, standard antibiotics, and the DMSO control. This initial screening provides insight into the comparative antibacterial efficacy of the synthesized compounds relative to conventional drugs.

Table 3. Results of the diameter of the studied ligand 3 inhibition zone and antibiotics, and
DMSO.

	Diameter of the zone inhibition (mm)									
_	Staphylococcus	Salmonella	Listeria	E-coli						
	aureus									
3 (Ligand)	nd	nd	nd	nd						
4 (mono Fe-Complex)	nd	nd	nd	10.00 ± 2.65						
5 (di Fe-Complex)	nd	nd	nd	11.50 ± 4.95						
6 (Zn-Complex)	7.00	8.00	8.00	$8.50 \pm 0.71$						
7 (Co-Complex)	7.67 ± 0.71	8.33 ± 0.58	9.00 ± 1.41	11.33 ± 3.51						
8 (Cu-Complex)	nd	nd	nd	nd						
Gentamycin	30.00	30.00	30.00	45.00						
DMSO	0.00	0.00	0.00	0.00						

The antibacterial activities of ligand 3 and its metal complexes (4-8) were assessed against both Gram-positive and Gram-negative bacteria by measuring the diameter of inhibition zones formed around the disks (**Table 3**). The data revealed selective and varied antibacterial effects among the tested compounds:

- (i) Ligand 3 demonstrated notable antibacterial activity, particularly against Escherichia coli, as indicated by a clear zone of inhibition. However, no inhibition zones were observed against the Gram-positive strains Staphylococcus aureus and Listeria monocytogenes, or the Gram-negative strain Salmonella, suggesting selective antibacterial efficacy of the free ligand, possibly due to its structural compatibility with the E. coli outer membrane.
- (ii) In contrast, the metal complexes (4-8) exhibited broader antibacterial activity, with measurable inhibition zones against both Gram-positive and Gram-negative strains. Specifically, complexes 4 (mono-Fe) and 5 (di-Fe) showed inhibition zones of  $10.00 \pm 2.65$  mm and  $11.50 \pm 4.95$  mm, respectively, against E. coli. However, they were ineffective against Staphylococcus aureus, Listeria, and Salmonella, showing no inhibition zones for those strains.
- (iii) Complex 6 (Zn) displayed moderate antibacterial activity, with inhibition zones of  $8.50 \pm 0.71 \, \text{mm}$  and  $8.00 \, \text{mm}$  against E. coli and Salmonella, respectively. It also showed activity against Gram-positive strains, producing inhibition zones of  $8.00 \, \text{mm}$  for Listeria and  $7.00 \, \text{mm}$  for Staphylococcus aureus.
- (iv) Complex 7 (Co) demonstrated the broadest spectrum among all complexes, with zones of inhibition measuring  $11.33 \pm 3.51$  mm and  $8.33 \pm 0.58$  mm for E. coli and Salmonella (Gram-negative), and  $9.00 \pm 1.41$  mm and  $7.67 \pm 0.71$  mm for Listeria and Staphylococcus aureus (Gram-positive), respectively. This suggests moderate to strong efficacy across all bacterial types.
- (v) Complex 8 (Cu) showed limited antibacterial performance. No inhibition zones were observed against Salmonella, while only weak activity was recorded against other strains [40,41].

These findings highlight that metal complexation enhances the antibacterial spectrum of the ligand, particularly for Co(II)-based systems. The variation in activity may be attributed to differences in metal-ligand coordination geometry, lipophilicity, and membrane permeability of each complex.

**Table 4.** The minimum inhibitory concentration obtained by the micro-dilution method of complexes from 4 to 8.

			3	4	5	6	7	8
v	Si	1	nd	nd	nd	+	+	nd
	Staphylococcu s aureus	10	nd	nd	nd	+	+	nd
	hyl auı	50	nd	nd	nd	+	+	nd
	phyloco s aureus	100	nd	nd	nd	+	+	nd
0	S	250	nd	nd	nd	-	-	nd
Concentration minimal inhibitrice $mg/ml$	_	500	nd	nd	nd	-	-	nd
cer		1	nd	nd	nd	+	+	nd
tra	Salmonella	10	nd	nd	nd	+	+	nd
atic	mo	50	nd	nd	nd	+	+	nd
ă	ne	100	nd	nd	nd	+	+	nd
ᇍ	lla	250	nd	nd	nd	-	-	nd
₫.		500	nd	nd	nd	-	-	nd
a		1	nd	nd	nd	+	+	nd
h	_	10	nd	nd	nd	+	+	nd
햜	Listeria	50	nd	nd	nd	+	+	nd
iric	ria	100	nd	nd	nd	+	+	nd
ë		250	nd	nd	nd	-	+	nd
ng/		500	nd	nd	nd	-	-	nd
<u>3</u>		1	nd	+	+	+	+	nd
	_	10	nd	+	+	+	+	nd
	E.coli	50	nd	=	-	+	+	nd
	≌:	100	nd	-	-	+	-	nd
		250	nd	-	-	-	-	nd
		500	nd	-	-	-	-	nd

The minimum inhibitory concentration (MIC) values for ligand 3 and its corresponding metal complexes (4–8) were determined against both Gram-positive and Gram-negative bacterial strains. The results, summarized in **Table 4**, reveal clear distinctions in antibacterial potency and selectivity.

For ligand 3, MIC values appeared similar across both bacterial classes. However, despite its visible zones of inhibition, ligand 3 did not exhibit measurable inhibitory concentrations against Staphylococcus aureus, Listeria, Salmonella, or E. coli. This suggests that while the ligand shows some surface-level antimicrobial effects, it lacks the potency to inhibit bacterial proliferation under MIC conditions, thereby reflecting selective and non-bactericidal activity. In contrast, the metal complexes demonstrated more defined MIC profiles:

- (i) Complexes 4 (mono-Fe) and 5 (di-Fe) exhibited MIC values of 50 mg/mL exclusively against E. coli, indicating selective efficacy against Gram-negative bacteria. No inhibition was observed against the other strains.
- (ii) Complex 6 (Zn) showed broader but weaker activity, with a MIC of 250 mg/mL against E. coli, Salmonella, Staphylococcus aureus, and Listeria, suggesting moderate, non-selective efficacy.

- (iii) Complex 7 (Co) exhibited the most consistent antibacterial activity across all tested strains: MIC values of 250 mg/mL against E. coli, Salmonella, and Staphylococcus aureus, and 500 mg/mL against Listeria. This indicates modest but broad-spectrum activity.
- (iv) Complex 8 (Cu) showed no measurable MIC against any tested strains, suggesting a lack of significant antibacterial effect.

The comparative MIC analysis highlights complex 7 (Co) as the most promising antibacterial agent due to its consistent activity across both Gram-positive and Gram-negative strains. This is followed by complex 6 (Zn), which also exhibited multi-strain effectiveness, though at a higher MIC threshold.

In contrast, complexes 4 and 5 (Fe) showed selective activity against E. coli, a Gramnegative bacterium, but had no detectable effect on Gram-positive strains, indicating metal-dependent selectivity. Notably, complex 8 (Cu) failed to inhibit any of the tested strains, confirming its lack of antibacterial potential.

These trends affirm that the nature of the central metal ion plays a crucial role in modulating antibacterial activity. Cobalt(II) coordination appears to enhance membrane interaction or bioavailability, explaining its broader effect. Conversely, copper(II) complexes may possess unfavorable structural or electronic features that limit their interaction with microbial targets [26,42].

Moreover, although ligand 3 alone did not demonstrate significant MIC-based efficacy, its complexation with Fe and Zn improved selective or modest activity. These findings suggest that metal—ligand design tuning could optimize antibacterial properties for future therapeutic applications.

To evaluate the drug-likeness and pharmacokinetic properties of ligand 3 and its metal complexes (4–8), SWISS ADMET prediction tools were employed. The analysis included key parameters: absorption, distribution, metabolism, excretion, and toxicity (ADMET), all of which are critical for assessing the therapeutic viability of newly synthesized compounds.

The BOILED-Egg model was used as a visual tool to predict gastrointestinal (GI) absorption and blood—brain barrier (BBB) permeability. This model classifies compounds based on lipophilicity and polarity into distinct absorption/distribution regions, offering insights into oral bioavailability and CNS activity potential [43].

**Figures 8** and **9** display the BOILED-Egg plots for ligand 3 and its complexes, respectively. These figures highlight the predicted differences in passive GI absorption and BBB penetration across the compound series.

The pharmacological and pharmacokinetic properties of ligand 3 and its corresponding metal complexes (4–8) were comprehensively evaluated using the SwissADME web tool. This in silico analysis provided critical insights into multiple parameters that influence drug-likeness and therapeutic viability. Key properties assessed included:

- (i) Aqueous solubility,
- (ii) Gastrointestinal (GI) absorption,
- (iii) Blood-brain barrier (BBB) permeability,
- (iv) Skin permeability,
- (v) Cytochrome P450 (CYP) enzyme inhibition,
- (vi) Lipophilicity (Log P),
- (vii) and other ADMET-related descriptors.

These parameters are essential for predicting oral bioavailability, systemic distribution, metabolic stability, potential for drug-drug interactions, and overall safety of the synthesized compounds.

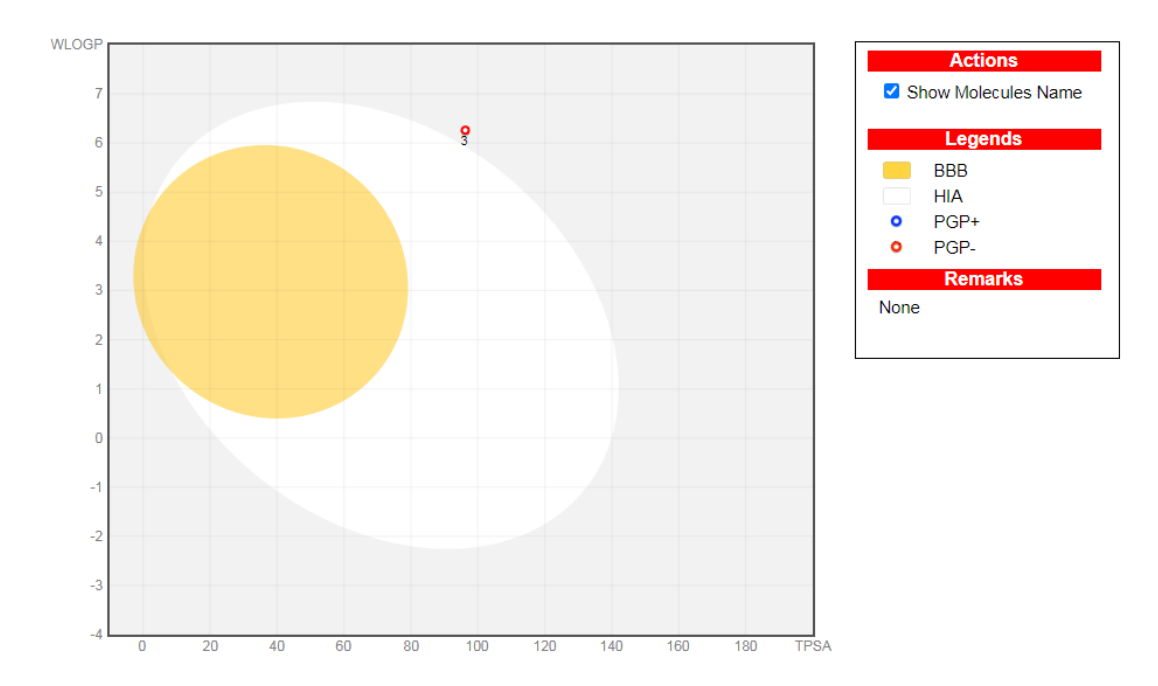


Figure 8. BOILED-Egg represents gastrointestinal absorption and brain penetration of ligand.

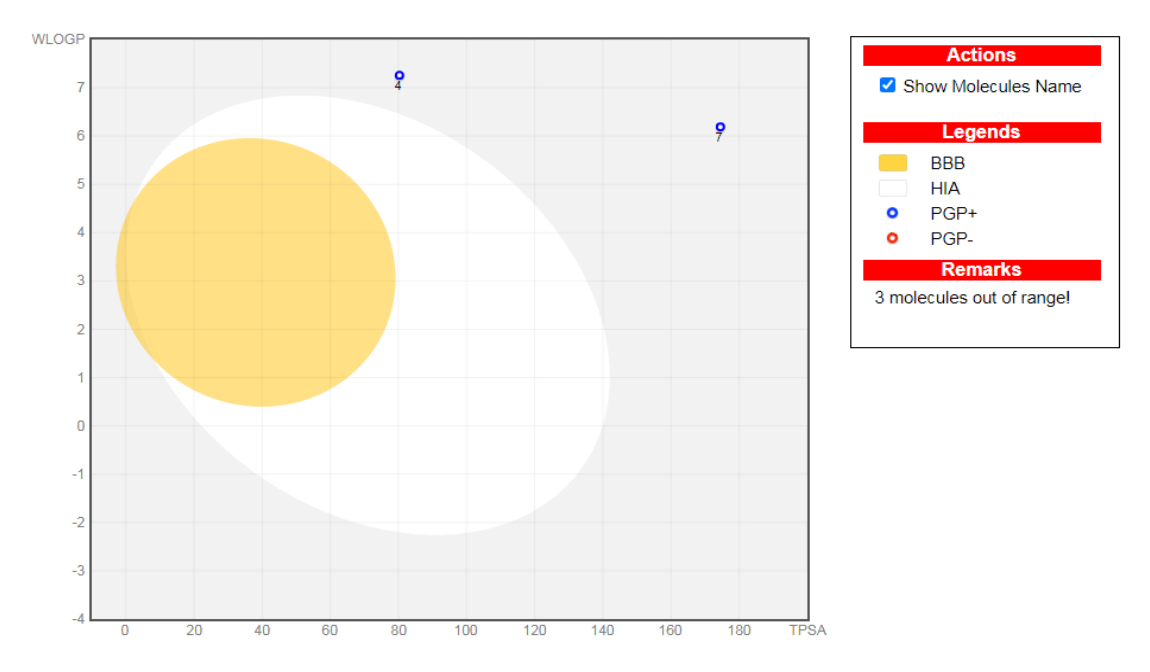


Figure 9. BOILED-Egg represents gastrointestinal absorption and brain penetration of complexes from 4 to 8.

The results, summarized in **Table 5**, reveal distinct differences in pharmacokinetic behavior between the free ligand and its metal complexes. The analysis offers valuable direction for future structural modifications aimed at improving bioavailability and metabolic compatibility.

**Table 5.** Represents pharmacokinetics and similarity calculations carried out by Swiss ADMET for ligand 3 and complexes from 4 to 8. (N: No. Y: Yes).

Compounds	MW (g/mol)	S gol	Gl absorption	BBB permeant	Log Kp (cm/s)	CYP1A2	CYP2C19 Inhibitor	CYP2C9	CYP2D6	CYP3A4 Inhibitor	log Po/w	Lipinski # Violation	PAINS
3 (Ligand)	676.85	-8.12	Low	N	-5.39	N	Υ	Υ	N	Υ	5.36	N; 2	0
4 (mono Fe- Complex)	803.62	-11.15	Low	N	-3.90	N	Υ	N	N	Υ	4.57	N; 2	0
5 (di Fe- Complex)	930.36	-14.19	Low	N	-2.41	N	N	N	N	Υ	4.87	N; 2	0
6 (Zn-Complex)	939.90	-14.25	Low	N	-2.47	N	Ν	Ν	N	Υ	4.88	N; 2	0
7 (Co-Complex)	986.56	-13.83	Low	N	-3.21	Ν	N	Ν	N	Υ	2.62	N; 2	0
8 (Cu-Complex)	938.06	-14.23	Low	N	-2.46	N	N	N	N	Υ	4.88	N; 2	0

The pharmacokinetic profiles of ligand 3 and its metal complexes (4–8) were predicted using the SwissADMET web server. This computational tool provides insights into absorption, distribution, metabolism, excretion, and toxicity (ADMET), as well as drug-likeness filters, thereby supporting early-stage assessment of therapeutic viability.

To assess gastrointestinal (GI) absorption and blood—brain barrier (BBB) permeability, the BOILED-Egg model was applied. As shown in **Figures 8** and **9**, ligand 3 was positioned in the white region, indicating good GI absorption and non-penetration of the BBB (PGP—). Complexes 4 (mono-Fe) and 7 (Co) also appeared in the white region, reflecting similarly favorable GI absorption, although both were flagged as PGP+, suggesting possible efflux by P-glycoprotein transporters.

Interestingly, complexes 5, 6, and 8 were not represented in the model output, likely due to molecular property constraints that exceed the predictive limits of the algorithm. Their absence emphasizes the limitations of the BOILED-Egg model and the need for complementary predictive tools to evaluate large, complex molecules [19,20].

Further pharmacokinetic parameters predicted by SwissADMET are summarized in Table 5. All compounds exhibited molecular weights above 676 g/mol, with complex 7 (Co) being the heaviest (986.56 g/mol). High molecular weight is commonly associated with poor membrane permeability and reduced oral bioavailability.

Solubility (log S) values were also unfavorable. Ligand 3 presented a low solubility of -8.12, while complexes 5, 6, and 8 exhibited even poorer solubility, ranging from -14.19 to -14.25, raising concerns for formulation feasibility.

In terms of GI absorption, all compounds were predicted to have low absorption rates, limiting their systemic bioavailability. Moreover, none of the compounds showed BBB penetration, restricting their utility for central nervous system targets.

Regarding cytochrome P450 (CYP450) interactions, ligand 3 and complex 4 were predicted to inhibit CYP2C19 and CYP3A4, indicating a potential for drug—drug interactions. In contrast, complexes 5–8 did not significantly inhibit any major CYP enzymes, suggesting lower interaction risk (Dascălu et al. 2020).

Analysis of lipophilicity (log Po/w) showed that ligand 3 was the most lipophilic (5.36), which may promote partitioning into lipid-rich environments. Complexes exhibited lower values: complex 7 (Co) had the lowest lipophilicity (2.62), while complexes 6 and 8 were moderately lipophilic (4.88).

All compounds violated two of Lipinski's rules, primarily due to high molecular weight and poor solubility, suggesting limitations in their oral drug-likeness [44].

Overall, ligand 3 demonstrated favorable lipophilicity but was hampered by low solubility and poor absorption, limiting its bioavailability. Among the metal complexes, complexes 4 (mono-Fe) and 7 (Co) emerged as the most pharmacokinetically viable, showing better predicted GI absorption. In contrast, complexes 5, 6, and 8 face significant formulation and delivery challenges, requiring further optimization for therapeutic application.

To investigate the structure—activity relationship (SAR) and potential binding modes of the synthesized compounds, molecular docking simulations were performed against the P-glycoprotein receptor (PDB: 4Z2D) (see **Figure 10**). This approach aimed to compare the interaction profiles of ligand 3 and complexes 4 to 8, identify potential antimicrobial binding mechanisms, and validate their target-specificity at the molecular level.

Details of binding affinity, interaction energies, and docking configurations are discussed in the next section, further contextualizing the antimicrobial activities observed in biological assays.

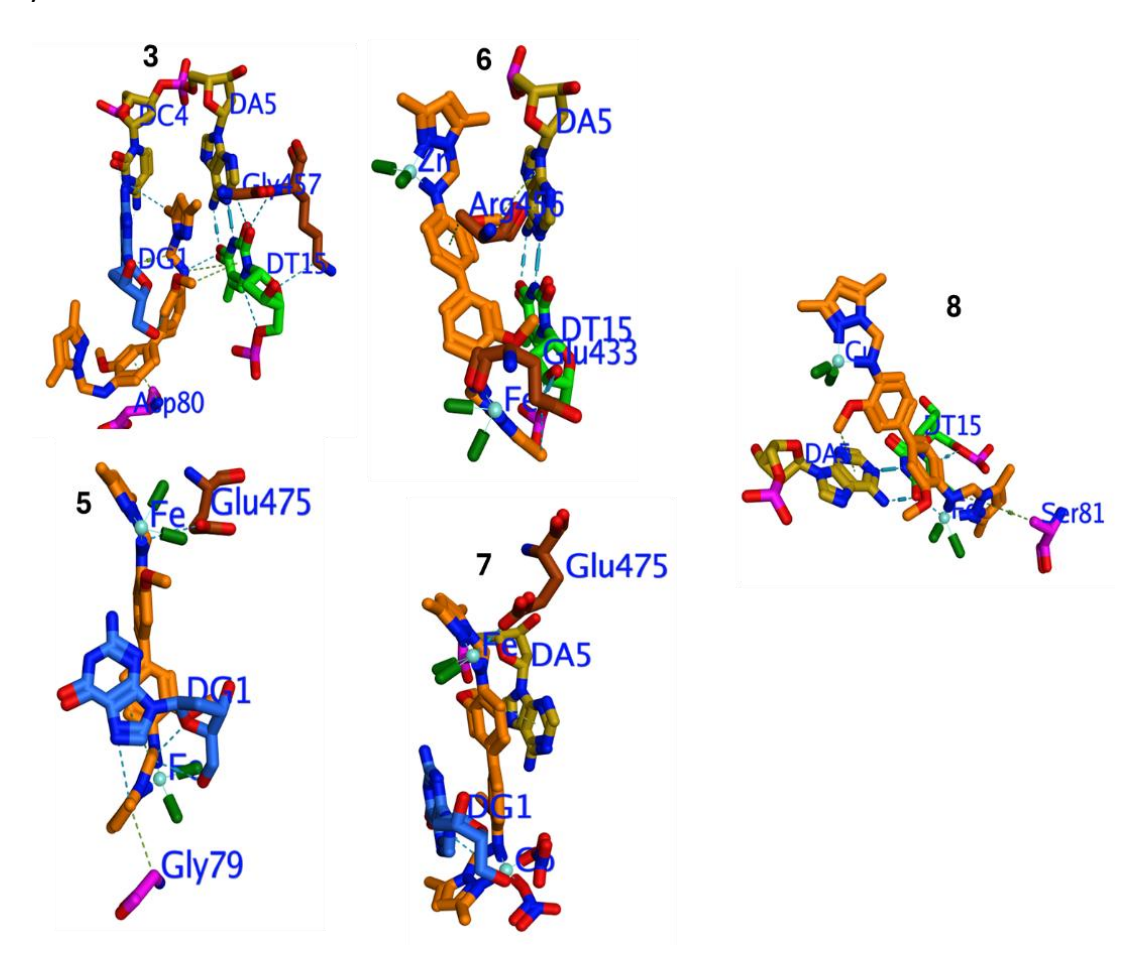


Figure 10. Molecular docking.

Molecular docking simulations were performed to assess the interaction potential [34,45-57]. Specifically, it is for ligand 3 and its metal complexes (4–8) with the P-glycoprotein receptor (PDB: 4Z2D). The docking results offer valuable insight into their structure—activity relationships (SAR) and potential as antimicrobial agents.

Key parameters analyzed include binding affinity, interaction energy, and hydrogen bonding strength, as summarized in the following:

(i) Binding Affinity and Molecular Ranking. The compounds were ranked based on binding affinity (kcal/mol) as follows: 5 (Di Fe-complex) (-20.74) > 8 (Cu-complex) (-14.89) > 3 (Ligand) (-12.05) > 4 (Mono Fe-complex) (-11.78) > 6 (Zn-complex) (-9.64) > 7 (Co-

- complex) (–8.59). These results indicate that di-Fe complexation (5) substantially enhances binding affinity, positioning it as the most potent candidate in terms of molecular interaction with the target protein. Copper complexation (8) also improves binding affinity relative to the free ligand, whereas zinc (6) and cobalt (7) complexes reduce binding affinity, suggesting lower predicted antimicrobial efficacy.
- (ii) Interaction Energy. Interaction energy values further illustrate the differential binding performance of the compounds: the strongest interaction energies are −12.19 kcal/mol (5, Di Fe)
- (iii) -12.08 kcal/mol (7, Co); and the weakest interaction energy: -8.73 kcal/mol (8, Cu).
- (iv) Hydrogen bonding. Hydrogen bonding energies reveal a different trend: The strongest H-bonding:
- (v) -34.49 kcal/mol (6, Zn) > -34.10 kcal/mol (5, Di Fe) > -33.49 kcal/mol (8, Cu). The weakest H-bonding: -10.07 kcal/mol (7, Co). These data suggest a trade-off in coordination effects: while zinc and copper complexes strengthen hydrogen bonding, they may compromise overall binding affinity or interaction energy.
- (vi) Impact of Metal Coordination. The SAR analysis shows that iron coordination, particularly in di-nuclear form (complex 5), significantly enhances all three parameters (binding affinity, interaction energy, and hydrogen bonding). This indicates a strong potential for Fe(II)-based complexes in antimicrobial drug design. Compared to the mono-Fe complex (4), complex 5 benefits from dual metal centers, which may increase the number of interaction sites and stabilize the binding conformation. Copper coordination (8) also improves both binding affinity and hydrogen bonding, albeit at the cost of a slight reduction in interaction energy. This suggests a moderate enhancement of activity. Conversely, zinc coordination (6) improves hydrogen bonding but lowers affinity, while cobalt coordination (7) yields the weakest performance in both binding affinity and H-bonding, though its interaction energy remains high; highlighting potential inefficiencies in geometric or electrostatic complementarity with the protein [48,49].
- (vii) Implications for Antimicrobial Design. Overall, the docking analysis confirms that metal complexation plays a critical role in modulating protein—ligand interactions. The choice of metal ion significantly impacts binding strength, interaction mechanisms, and bioactivity potential. The Di Fe-complex (5) consistently ranks highest across all evaluated parameters, making it the most promising candidate for further development as an antimicrobial agent. These findings highlight the need for rational design strategies that integrate metal selection, ligand optimization, and target compatibility to enhance the pharmacological performance of metal-based antimicrobial compounds.

This study on pyrazole-based tetradentate ligands and their transition metal complexes has yielded significant outcomes in both fundamental coordination chemistry and applied catalysis and biomedical research. The successful synthesis of ligand 3 and its metal complexes with Fe(II), Zn(II), Co(II), and Cu(II) was confirmed through comprehensive spectroscopic and structural analyses, including UV-Vis, IR, NMR, mass spectrometry, and X-ray crystallography. These techniques allowed for the precise determination of coordination environments and structural integrity.

Catalytic investigations revealed that the synthesized complexes exhibit remarkable biomimetic activity in catechol oxidation reactions, with iron complexes, particularly the difference complexes, demonstrating catalytic performance comparable to that of natural enzymes. These results highlight their potential as green and sustainable catalysts in environmentally conscious chemical processes.

In parallel, antimicrobial evaluations showed promising biological activity, particularly against bacterial and fungal pathogens, including drug-resistant strains. Notably, Co(II)- and Cu(II)-based complexes exhibited enhanced efficacy, likely due to improved interaction with biological membranes and protein targets. This positions them as viable candidates for the development of new antimicrobial therapeutics.

Furthermore, structure—activity relationship (SAR) analysis underscored the critical influence of metal identity, coordination geometry, and pyrazole substituents on both catalytic efficiency and biological activity. The combined results underline the versatility of pyrazole-derived metal complexes and their potential application in diverse domains, from biomimetic catalysis to medicinal chemistry.

Taken together, this work provides a strong foundation for future optimization strategies and offers promising perspectives in the search for innovative solutions to current challenges in public health, environmental sustainability, and therapeutic design.

#### 4. CONCLUSION

This study successfully synthesized and characterized pyrazole-based tetradentate ligands and their metal complexes with Fe(II), Zn(II), Co(II), and Cu(II). The complexes exhibited strong catalytic activity in catechol oxidation, mimicking natural enzymes, and demonstrated significant antimicrobial effects, especially the Co(II) and Cu(II) derivatives. Structure—activity analysis revealed that metal type and ligand coordination strongly influence performance. These findings highlight the dual potential of pyrazole-metal complexes in green catalysis and therapeutic applications. Overall, this research provides a valuable foundation for developing multifunctional compounds addressing both environmental and biomedical challenges through rational design and metal-ligand optimization.

#### 5. ACKNOWLEDGMENT

The authors gratefully acknowledge the support of University Mohammed Premier, Oujda, Morocco, and the Laboratory of the Higher Institute of Nursing and Health Techniques (ISPITS), Oujda, Morocco. Special thanks are extended to the Project CNRST / TUBITAK (2023–2025), a collaborative initiative between University Mohammed Premier, Morocco and Inonu University, Turkey, for their valuable financial and institutional support throughout the course of this research.

#### 6. AUTHORS' NOTE

The authors declare that there is no conflict of interest regarding the publication of this article. Authors confirmed that the paper was free of plagiarism.

# 7. REFERENCES

- [1] Chougule, M. A., Pawar, S. G., Godse, P. R., Mulik, R. N., and Sen, S. (2011). Synthesis and characterization of polypyrrole (PPy) thin films. *Scientific Notes Letters*, 1(1), 6–10.
- [2] Ambarwati, N. S. S., Sukma, N. T., Desmiaty, A. A. Y., Budi, M. A. S., and Ahmad, I. (2024). Molecular docking studies and ADME-Tox prediction of phytocompounds from *Merremia peltata* as a potential anti-alopecia treatment. *Journal of Advanced Pharmaceutical Technology & Research*, 15(1), 8–12.

- [3] Claiborne, A., and Fridovich, I. (2020). Chemical and enzymatic intermediates in the peroxidation of o-dianisidine by horseradish peroxidase. *Educational Activity Programs* for Older Adults, 18, 2324–2329.
- [4] Rydosz, A. (2018). The use of copper oxide thin films in gas-sensing applications. *Coatings*, 8(12), 425.
- [5] Fayomi, O. S. I., and Popoola, A. P. I. (2015). Anti-corrosion properties and structural characteristics of fabricated ternary coatings. *Surface Engineering and Applied Electrochemistry*, *51*(1), 76–84.
- [6] Ouadi, Y. E., Bouratoua, A., Bouyenzer, A., Kabouche, Z., Touzani, R., El Msellem, H., Hammouti, B., and Chetouani, A. (2015). Effect of *Athamanta sicula* oil on inhibition of mild steel corrosion in 1M HCl. *Scholars Research Library, 7*(March), 103–111.
- [7] Bahriz, H., and Bouras, N. (2020). Study of Bayoud's disease and the varietal behavior of the date palm against *Fusarium oxysporum* f. sp. *albedinis* in the Mzab Valley A. *African Review of Science, Technology and Development, 5*(1), 41–60.
- [8] Belfilali, I., and Roisnel, T. (2024). Catecholase activity assessment of in-situ copper complexes derived from a novel Schiff base ligand. *Inorganic Chemistry Communications*, 164(II), 1–15.
- [9] Radi, S., Salhi, S., and Radi, A. (2009). Synthesis and preliminary biological activity of some new pyrazole derivatives as acyclonucleoside analogues. *Letters in Drug Design & Discovery*, 7(1), 27–30.
- [10] Kaddouri, Y., Benabbes, R., Ouahhoud, S., Abdellattif, M., Hammouti, B., and Touzani, R. (2022). An insight into all tested small molecules against *Fusarium oxysporum* f. sp. *albedinis*: A comparative review. *Molecules*, *27*(9), 1–21.
- [11] Karrouchi, K., Charkaoui, Y., Benlafya, K., Ramli, Y., Taoufik, J., Radi, S., & Ansar, M. (2013). Synthesis, characterization and preliminary biological activity of some new pyrazole carbohydrazide derivatives. *Journal of Chemical and Pharmaceutical Research*, 5(3), 1–6.
- [12] Boutaybi, M. E., Bouroumane, N., Azzouzi, M., Aaddouz, M., Bacroume, S., El Miz, M., and Touzani, R. (2023). Synthesis, characterization, DFT, and thermogravimetric analysis of neutral Co(II)/pyrazole complex, catalytic activity toward catecholase and phenoxazinone oxidation. *Crystals*, 13, 155.
- [13] Messali, M., Ati, R. E., Touzani, R., Aouad, M. R., and Warad, I. (2018). Crystal structure of the coordination polymer catena-poly [chlorido-{μ2-2-(((3, 5-dimethyl-1 H-pyrazol-1-yl) methyl) amino)-3-hydroxybutanoato-κ4 N, N, O: O'} copper (II)], C11H16ClCuN2O3. Zeitschrift für Kristallographie-New Crystal Structures, 233(3), 493-494.
- [14] Setifi, F., Moon, D., Koen, R., Setifi, Z., Lamsayah, M., and Touzani, R. (2016). Crystal structure of bis(azido-κN)bis(quinolin-8-amine-κ²N,N′)iron(II). *Acta Crystallographica Section E: Crystallographic Communications, 72*, 1488–1491.
- [15] Titi, A., Messali, M., Touzani, R., Fettouhi, M., Zarrouk, A., Al-Zaqri, N., and Warad, I. (2020). Synthesis of Novel Tetra (μ3-Methoxo) Bridged with [Cu (II)-O-Cd (II)] Double-Open-Cubane Cluster: XRD/HSA-Interactions, Spectral and Oxidizing Properties. *International Journal of Molecular Sciences*, *21*(22), 8787.
- [16] Benzai, A., Derridj, F., El Ati, R., El Kodadi, M., Touzani, R., Aouniti, A., Hammouti, B., Ben Hadda, T., and Doucet, H. (2019). Studies of catecholase activities of N-donor bidentates ligands derivated from benzoxazole with copper (II) salts. *Moroccan Journal of Chemistry*, 7(2), 401–409.

- [17] Zeghib, L. S., Kabouche, A., Semra, Z., Smati, F., Touzani, R., and Kabouche, Z. (2013). Composition, antibacterial and antioxidant activity of the essential oil of *Thymus numidicus* Poiret from Constantine (Algeria). *Der Pharmacia Lettre*, 5, 206–210.
- [18] Touzani, R., Ramdani, A., Ben-Hadda, T., El Kadiri, S., Maury, O., Le Bozec, H., and Dixneuf, P. H. (2001). Efficient synthesis of new nitrogen donor containing tripods under microwave irradiation and without solvent. *Synthetic Communications*, *31*(9), 1315–1321.
- [19] Várnagy, K., Bóka, B., Sóvágó, I., Sanna, D., Marras, P., and Micera, G. (1998). Potentiometric and spectroscopic studies on the copper(II) and nickel(II) complexes of tripeptides of methionine. *Inorganica Chimica Acta, 275–276*, 440–446.
- [20] Go, Y. B., Wang, X., Anokhina, E. V., and Jacobson, A. J. (2004). A chain of changes: Influence of noncovalent interactions on the one-dimensional structures of nickel(II) dicarboxylate coordination polymers with chelating aromatic amine ligands. *Inorganic Chemistry*, *43*(17), 5360–5367.
- [21] Amundsen, A. R., Whelan, J., and Bosnich, B. (1977). Biological analogues: On the nature of the binding sites of copper-containing proteins. *Journal of the American Chemical Society*, 99(20), 6730–6739.
- [22] Aust, S. D., Morehouse, L. A., and Thomas, C. E. (1985). Role of metals in oxygen radical reactions. *Journal of Free Radicals in Biology and Medicine*, 1(1), 3–25.
- [23] Moiseeva, A. A., and Butin, K. P. (2005). Complexation in a 5-acylpyrimidine-4-thione—aliphatic diamine—metal(II) chloride system (M = Ni or Co): The molecular structure of fac tris(5-acetyl-2,4-dimethylpyrimidine-6-thiolato)cobalt(III). *Russian Journal of Coordination Chemistry*, 54(12), 2757–2770.
- [24] Groysman, S., and Holm, R. H. (2009). Biomimetic chemistry of iron, nickel, molybdenum, and tungsten in sulfur-ligated protein sites. *Biochemistry*, 48(11), 2310–2320.
- [25] Holland, P. L., Tolman, W. B., & Se, P. S. (2000). A structural model of the type 1 copper protein active site. *Journal of the American Chemical Society*, 1(II), 6331–6332.
- [26] Manessi-Zoupa, E., Perlepes, S. P., Hondrellis, V., and Tsangaris, J. M. (1994). Transition metal complexes of N-(2-benzamide)pyridine-2'-carboxamide: Preparation and characterization in the solid state. *Journal of Inorganic Biochemistry*, 55(3), 217–233.
- [27] Prousek, J. (2007). Fenton chemistry in biology and medicine. *Pure and Applied Chemistry*, 79(12), 2325–2338.
- [28] Yassine, K., Abrigach, F., Ouahhoud, S., Benabbes, R., El Kodadi, M., Alsalme, A., Al-Zaqri, N., Warad, I., and Touzani, R. (2020). Mono-alkylated ligands based on pyrazole and triazole derivatives tested against *Fusarium oxysporum* f. sp. *albedinis*. *Frontiers in Chemistry*, 8, 1–18.
- [29] Gupta, R., Raza, A., Singh, S. K., Kaur, J., and Wadhwa, P. (2024). Computational evaluation of ADMET properties and molecular docking studies on cryptolepine analogs as inhibitors of HIV integrase. *Current Signal Transduction Therapy*, 19, 1–26.
- [30] Gu, Y., Yu, Z., Wang, Y., Chen, L., Lou, C., Yang, C., Li, W., Liu, G., and Tang, Y. (2024). AdmetSAR3.0: A comprehensive platform for exploration, prediction and optimization of chemical ADMET properties. *Nucleic Acids Research*, *52*(April), W432–W438.
- [31] Masoud, M. S., Yacout, G. A., Abd-El-Khalek, B. A., and Ramadan, A. M. (2023). Synthesis, physicochemical characterization, biological assessment, and molecular docking study of some metal complexes of alloxan and ninhydrin as alterdentate ligands. *Journal of Inorganic and Organometallic Polymers and Materials*, 33(8), 2252–2269.

- [32] El Moussaoui, A., Jawhari, F. Z., Almehdi, A. M., Elmsellem, H., Benbrahim, K. F., Bousta, D., and Bari, A. (2019). Antibacterial, antifungal and antioxidant activity of total polyphenols of *Withania frutescens*. *Bioorganic Chemistry*, *93*, 103337.
- [33] Abdel Rahman, S. M., Abd-Ellatif, S. A., Deraz, S. F., and Khalil, A. A. (2011). Antibacterial activity of some wild medicinal plants collected from western Mediterranean coast, Egypt: Natural alternatives for infectious disease treatment. *African Journal of Biotechnology*, 10(52), 10733–10743.
- [34] Diass, K., Merzouki, M., Elfazazi, K., Azzouzi, H., Challioui, A., Azzaoui, K., Hammouti, B., et al. (2023). Essential oil of *Lavandula officinalis*: Chemical composition and antibacterial activities. *Plants*, *12*, 1571.
- [35] Bouammali, H., Zraibi, L., Ziani, I., Merzouki, M., Bourassi, L., Fraj, E., and Challioui, A.. (2024). Rosemary as a potential source of natural antioxidants and anticancer agents: A molecular docking study. *Plants*, *13*, 1–18.
- [36] Nakajima, Y., Takeshita, T., and Jheng, N. Y. (2021). Metal-ligand cooperation behaviour of Fe and Co complexes bearing a tetradentate phenanthroline-based PNNP ligand. *Dalton Transactions*, *50*(22), 7532–7536.
- [37] Sogukomerogullari, H. G., Yalçin, Ş. P., Ceylan, Ü., Aytar, E., Aygün, M., Richeson, D. S., and Sönmez, M. (2019). Synthesis of Fe and Cu metal complexes derived from 'SNS' pincer type ligands and their efficient catalyst precursors for the chemical fixation of CO<sub>2</sub>. *Journal of Chemical Sciences*, 131(4), 53.
- [38] Holm, R. H., Kennepohl, P., and Solomon, E. I. (1996). Structural and functional aspects of metal sites in biology. *Chemical Reviews*, *96*(7), 2239–2314.
- [39] Ibers, J. A., and Holm, R. H. (1980). Modeling coordination sites in N-Zn-. *Science*, 209(4453), 223–235.
- [40] Jazdzewski, B. A., Holland, P. L., Pink, M., Young, V. G., Spencer, D. J. E., & Tolman, W. B. (2001). Three-coordinate copper(II)-phenolate complexes. *Inorganic Chemistry*, 40(24), 6097–6107.
- [41] Knoblauch, S., Benedix, R., Ecke, M., Gelbrich, T., Sieler, J., Somoza, F., and Hennig, H. (1999). Synthesis, crystal structure, spectroscopy, and theoretical investigations of tetrahedrally distorted copper(II) chelates with [CuN2S2] coordination sphere. *European Journal of Inorganic Chemistry, (8)*, 1393–1403.
- [42] Li, Y., Li, Z., Liu, Y., Dong, X., and Cui, Y. (2012). Synthesis, crystal structures, and urease inhibition studies of two new Schiff-base copper complexes derived from n-butylamine. *Journal of Coordination Chemistry*, 65(1), 19–27.
- [43] Raza, A., Chaudhary, J., Khan, A. A., Singh, M., Kumar, D., Malik, A., and Wadhwa, P. (2024). Exploring molecular interactions and ADMET profiles of novel MAO-B inhibitors: Toward effective therapeutic strategies for neurodegenerative disorders. *Future Journal of Pharmaceutical Sciences*, 10, 1–11.
- [44] Niu, Z., Xiao, X., Wu, W., Cai, Q., Jiang, Y., Jin, W., and Wang, M. (2024). PharmaBench: Enhancing ADMET benchmarks with large language models. *Scientific Data*, 11(1), 1–16.
- [45] El Mrayej, H., En-Nabety, G., Ettahiri, W., Jghaoui, M., Sabbahi, R., Hammouti, B., Rais, Z. and Taleb, M. (2025). Triazolopyrimidine derivatives: A comprehensive review of their synthesis, reactivity, biological properties, and molecular docking studies. *Indonesian Journal of Science and Technology*, 10(1), 41-74.
- [46] Merzouki, M., Khibech, O., Fraj, E., Bouammali, H., Bourhou, C., Hammouti, B., Bouammali, B., and Challioui, A. (2025). Computational engineering of malonate and tetrazole derivatives targeting SARS-CoV-2 main protease: Pharmacokinetics, docking, and molecular dynamics insights to support the sustainable development goals (SDGs),

- with a bibliometric analysis. *Indonesian Journal of Science and Technology, 10*(2), 399-418.
- [47] Alshahateet, S.F., Al-Trawneh, S.A., Hidaoui, S., Mohammed, E., Zerrouk, M., Al-Saraireh, Y.M., Al-Tawarh, W.M., Hareedy, M.S., Al-Abadleh, A.A., Alshahateet, T.S., Azzaoui, K., Hammouti, B., and Warad, I. (2026). Structural characterization, Hirshfield surface analysis, and molecular docking of novel diquinoline derivatives as anti-tumor agents. *Indonesian Journal of Science and Technology*, 11(1), 127-148.
- [48] Mohanasundaram, S., Karthikeyan, P., Sampath, V., Anbazhagan, M., Prabhu, S. V., Khaled, J. M., and Thiruvengadam, M. (2024). Molecular docking, dynamics simulations, ADMET, and DFT calculations: Combined in silico approach to screen natural inhibitors of 3CL and PL proteases of SARS-CoV-2. *Cellular Microbiology*, 2024, 1–19.
- [49] Hadda, T. B., Rastija, V., AlMalki, F., Titi, A., Touzani, R., Mabkhot, Y. N., Khalid, S., Zarrouk, A., and Siddiqui, B. S. (2019). Petra/Osiris/Molinspiration and molecular docking analyses of 3-hydroxy-indolin-2-one derivatives as potential antiviral agents. *Current Computer-Aided Drug Design*, 16, 1–11.
- [50] Titi, A., Messali, M., Touzani, R., Fettouhi, M., Zarrouk, A., Al-Zaqri, N., Alsalme, A., Alharthi, F. A., Alsyahi, A., and Warad, I. (2020). Synthesis of novel tetra (μ₃-methoxo) bridged [Cu(II)-O-Cd(II)] double-open-cubane cluster: XRD, spectral and oxidizing properties. International Journal of Molecular Sciences, 21, 8787.
- [51] Dascălu, D., Roman, D. L., Filip, M., Ciorsac, A., and Ostafe, V. (2020). Solubility and ADMET profiles of short oligomers of lactic acid. *International Journal of Molecular Sciences*, 8(4), 425–436.
- [52] Moiseeva, A. A., and Butin, K. P. (2005). Complexation in a 5-acylpyrimidine-4-thione—aliphatic diamine—metal(II) chloride system (M = Ni or Co): The molecular structure of fac tris(5-acetyl-2,4-dimethylpyrimidine-6-thiolato)cobalt(III). *Russian Journal of Coordination Chemistry*, 54(12), 2757–2770.
- [53] Hendrarti, W., Umar, A.H., Syahruni, R., Rafi, M., and Kusuma, W.A. (2024). Deciphering the mechanism of action cosmos caudatus compounds against breast neoplasm: A combination of pharmacological networking and molecular docking approach with bibliometric analysis. *Indonesian Journal of Science and Technology*, *9*(2), 527-556.
- [54] Lu, S. Y., Jiang, Y. J., Lv, J., Wu, T. X., Yu, Q. S., and Zhu, W. L. (2010). Molecular docking and molecular dynamics simulation studies of GPR40 receptor—agonist interactions. *Journal of Molecular Graphics and Modelling*, 28(8), 766-774.
- [55] Erdogan, T. (2021). DFT, molecular docking and molecular dynamics simulation studies on some newly introduced natural products for their potential use against SARS-CoV-2. *Journal of molecular structure*, *1242*, 130733.
- [56] Mohamed, G. A., Omar, A. M., El-Araby, M. E., Mass, S., and Ibrahim, S. R. (2023). Assessments of alpha-amylase inhibitory potential of tagetes flavonoids through in vitro, molecular docking, and molecular dynamics simulation studies. *International journal of molecular sciences*, 24(12), 10195.
- [57] Kushwaha, P. P., Singh, A. K., Bansal, T., Yadav, A., Prajapati, K. S., Shuaib, M., and Kumar, S. (2021). Identification of natural inhibitors against SARS-CoV-2 drugable targets using molecular docking, molecular dynamics simulation, and MM-PBSA approach. Frontiers in cellular and infection microbiology, 11, 730288.